Bonding, Thermodynamics and Dissociation Dynamics of NiO^+ and NiS^+ Determined by Photofragment Imaging and Theory

Schuyler P. Lockwood, Tala Chunga and Ricardo B. Metz*

Department of Chemistry, University of Massachusetts Amherst, Amherst, MA 01003

Email: rbmetz@chem.umass.edu Phone: +1-413-545-6089

Abstract

We use photofragment ion imaging and *ab initio* calculations to determine the bond strength and photodissociation dynamics of the nickel oxide (NiO^+) and nickel sulfide (NiS^+) cations. NiO^+ photodissociates broadly from 20350 to 32000 cm^{-1}, forming ground state products Ni^+ (^2D) + O (^3P) below ~29000 cm^{-1}. Above this energy, Ni^+ (^4F) + O (^3P) products become accessible and dominate over the ground state channel. In certain images, product spin-orbit levels are resolved, and spin-orbit propensities are determined. Image anisotropy and the results of MRCI calculations suggest NiO^+ photodissociates via a 3 $^4\Sigma^- \leftarrow$ X $^4\Sigma^-$ transition above the Ni^+ (^4F) threshold, and via 3 $^4\Sigma^-$, 2 $^4\Sigma^-$ and/or 2 $^4\Pi$ and 3 $^4\Pi$ excited states below the ^4F threshold. The photodissociation spectrum of NiS^+ from 19900 to 23200 cm^{-1} is highly structured, with ~12 distinct vibronic peaks, each containing underlying sub-structure. Above 21600 cm^{-1}, the Ni^+ ($^2D_{5/2}$) + S (^3P) and Ni^+ ($^2D_{3/2}$) + S (^3P) product spin-orbit channels compete, with a branching ratio of ~2:1. At lower energy, Ni^+ ($^2D_{5/2}$) is formed exclusively, and S ($^3P_2$) and S ($^3P_1$) spin-orbit channels are resolved. MRCI calculations predict the ground state of NiS^+ to be one of two nearly degenerate states, the 1 $^4\Sigma^-$ and 1 $^4\Delta$. Based on images and spectra, the ground state of NiS^+ is assigned as $^4\Delta_{7/2}$, with the 1 $^4\Sigma_{3/2}^-$ and 1 $^4\Sigma_{1/2}^-$ states 81 ± 30 and 166 ± 50 cm^{-1} higher in energy, respectively. The majority of the photodissociation spectrum is assigned to transitions from the 1 $^4\Delta$ state to two overlapping, predissociative excited $^4\Delta$ states. Our D_0 measurements for NiO^+ (D_0 = 244.6 ± 2.4 kJ/mol) and NiS^+ (D_0 = 240.3 ± 1.4 kJ/mol) are more precise and closer to each other than previously reported values. Finally, using a recent measurement of D_0 (NiS), we derive a more precise value for IE (NiS): 8.80 ± 0.02 eV (849 ± 1.7 kJ/mol).

I. Introduction

Several gas phase transition metal oxide cations (MO^+) activate methane and convert it to methanol at room temperature.[1–9] The most effective species for this reaction is NiO^+, converting methane to methanol with over 99% selectivity and 20% efficiency.[2,5] Transition metal sulfide cations (MS^+) do not activate methane[10] but do activate C-H bonds in larger hydrocarbons (as do most MO^+). For example, NiS^+ reacts with ethane to form a variety of neutral products, including ethene (51%), ethane thiol (11%) and H_2S (38%), while NiO^+ reacts to form only water and $NiC_2H_4^+$.[2,10] While experimental work has revealed important information about C-C and C-H bond activation by metal-containing ions (MX^+), it remains difficult to predict and model these reactions. MX^+ are very challenging molecules to treat theoretically, as they tend to have many unpaired electrons, numerous low-lying electronic states, and often can't be well described by a single electronic configuration. Ideally, efficient methods, such as Density Functional Theory (DFT) could be used to characterize these molecules, but the lack of accurate and precise experimental thermodynamic information on a wide variety of metal-containing molecules makes it hard to assess the accuracy of different functionals and approaches. Even fundamental properties like M^+-X bond dissociation energies (D_0) are often not known to useful precision, leaving large uncertainty in reaction thermodynamics and mechanistic feasibility.

There have been some experimental and theoretical studies of NiO^+ and NiS^+. Calculations, first by Nakao et al.[11] at the B3LYP and high level multi-reference configuration interaction (MRCI) level, and more extensive MRCI calculations by Sakellaris and Mavridis[12] unambiguously determined that the ground electronic state of NiO^+ is the $^4\Sigma^-$ state. The lowest-lying excited state was found to be the 1 $^4\Delta$, lying ~67 kJ/mol above the ground state.[12] These two states are also the two lowest lying in the isoelectronic NiS^+ molecule, but they are shifted significantly in energy relative to one another. B3LYP[13] and CCSD(T)[14] calculations predict that the ground state of NiS^+ is the 1 $^4\Delta$ state, lying only ~2-3 kJ/mol below the 1 $^4\Sigma^-$ state. The two states are so close in energy that the calculations do not determine the ground state. The few experimental studies of NiO^+ and NiS^+ suggest the oxide is more strongly bound. Armentrout and co-workers report[15] D_0 (NiO^+) = 260.7 ± 6.6 kJ/mol or more recently,[16] 254 ± 19 kJ/mol. The same group measured D_0 (NiS^+) = 237 ± 4 kJ/mol,[17] which agrees with a previous estimate of an upper limit by our group (D_0 (NiS^+) ≤ 238 ± 4 kJ/mol).[13] Theoretical values of D_0 (NiO^+)[11,12,18] and D_0 (NiS^+)[13,14] are all systematically lower than these experimentally measured values. It is worth noting the suggested trend in

oxide[15,16,19–26] and sulfide[17,27–30] D_0 values for Ni^+ is identical to that for Sc^+, Ti^+, V^+, Cr^+ Mn^+, Fe^+ and Co^+, but opposite Cu^+ and Zn^+. While the photodissociation spectrum of NiO^+ has not previously been measured, Hettich et al.[31] recorded the spectrum of NiS^+ from 230 to 480 nm using an arc lamp and monochromator with 10 nm resolution. More recently, our group[13] used a dye laser with 0.1 cm^{-1} linewidth to measure the spectrum from 20000 to 23000 cm^{-1}. The NiS^+ spectrum features a vibrational progression with 12 major peaks, each containing underlying spin-orbit structure. The reported[13] value of D_0 (NiS^+) $\leq$ 238 $\pm$ 4 kJ/mol is based on the observed fragmentation onset; uncertainty in the measurement considers the possibility that the observed onset results from photodissociation of hot ions.

Further experimental studies on the electronic structure and dynamics of NiO^+ and NiS^+ are needed to bolster theory and to better understand chemical bonding and thermodynamics in these systems. Photofragment velocity map imaging (VMI) has proven to be a useful experimental tool for measuring precise bond dissociation energies and dissociation dynamics in small molecules[32–37] and ions.[25,38–44] When complemented with spectroscopic measurements and theory, VMI gives an informative picture of how a photoexcited molecule moves around its potential energy surfaces. In this study, we probe the electronic structure, thermodynamics and photodissociation dynamics of NiO^+ and NiS^+ with a combination of theory, photofragment spectroscopy and ion velocity map imaging.

II. Methods

A. Experimental

The home-built photofragment imaging instrument used in these studies is described in detail elsewhere.[41] Nickel oxide and nickel sulfide cations are formed by laser ablating (2^{nd} harmonic of a Continuum Minilite II Nd:YAG laser) a rotating nickel disk in the presence of a gas mixture of either 10% O_2 in He (for NiO^+) or 0.5% CH_3SH in He (for NiS^+), introduced via a pulsed valve (Parker Series 9). Ions are then directed through a linear quadrupole ion guide into a refrigerated radiofrequency 3D quadrupole ion trap. A pulse of He or D_2 buffer gas is injected to help thermalize the ions to the trap temperature. After thermalizing with the buffer gas for ~55 ms, ions undergo Wiley-McLaren extraction and are accelerated to a kinetic energy of 1800 V; after

acceleration, the ions are re-referenced to ground potential. Ions are then mass selected by pulsing the voltage on a set of deflectors and are guided by a second set of deflectors into a reflectron.

For measuring photodissociation spectra, the ion beam interacts with the output of a pulsed dye laser (Continuum ND6000, 0.1 cm^{-1} linewidth); the dye laser is pumped by the second (532 nm) or third (355 nm) harmonic of a Nd:YAG laser (Continuum Powerlite 8020). The laser beam intersects the ion beam at the ions' turning point in the reflectron. The parent and resulting Ni^+ fragment signals are monitored with a microchannel plate (MCP) detector while scanning the dye laser wavelength. For photodissociating NiO^+, the dye laser fluence ranged from ~25 to 50 mJ/cm^2. For NiS^+, the dye laser fluence ranged from ~80 to 100 mJ/cm^2. Fluence was wavelength dependent, generally decreasing with increasing photon energy below 25000 cm^{-1} and generally increasing with increasing photon energy above 25000 cm^{-1}.

For photofragment imaging, the reflectron is grounded and the deflector voltages are tuned in order to direct the ion beam through an adjustable iris positioned after the reflectron. After passing through the iris, the beam enters a series of velocity map imaging (VMI) optics.[33] The parent ions are photolyzed between the first and second ion optic plates by the pulsed dye laser. Voltages on the first and second VMI optics are pulsed simultaneously with the laser to focus the newly formed fragment ions onto an imaging detector (coupled MCP-Phosphor screen, Photonis). In order to separate the two species in time, the fragment and remaining parent ions are accelerated between the second and third VMI optics. The imaging detector then receives a high voltage pulse sufficiently wide to capture all of the fragment ion signal and discriminate against the parent ions. Photofragment images are collected by a CCD camera facing the phosphor screen for ~20,000 to 100,000 laser shots. Images were measured with the ion trap at 55 K and He buffer gas for NiO^+, and at 80 K with D_2 buffer gas for NiS^+. Images are compiled with the *NuACQ* data acquisition software[45] and image analysis (fragment cloud reconstruction and kinetic energy analysis) is performed using the *BASEX* method.[46] The image anisotropy parameter (β) is determined using the Polar Onion-Peeling (POP) method.[47]

B. Theoretical

Calculations of the ground and several excited electronic states of NiO^+ and NiS^+ were carried out at the MRCI level using the *MOLPRO*[48,49] software package. For NiO^+ these calculations are very similar to those of Sakellaris and Mavridis,[12] but included additional excited

electronic states at higher energies, relevant to the experimental spectra. The MRCI calculations consist of a complete active space self-consistent field (CASSCF) calculation followed by single and double excitations from the active space. The CASSCF active space consists of the 4s and 3d orbitals on nickel and 2p on oxygen (13 electrons in 9 orbitals), and 12 quartet states of each symmetry are state averaged, with equal weights. For the MRCI, the active space is expanded to also allow promotions from the 2s orbital on oxygen, as was done by Sakellaris and Mavridis. The default, internally contracted (icMRCI) method was used. All calculations are carried out in C_{2v} symmetry, and states of each symmetry are calculated separately. The calculations use the aug-cc-pVQZ basis set for all atoms and include the Davidson correction, so they are at the MRCI+Q/aug-cc-pVQZ level.

For NiS^+, some potential energy curves using this active space do not dissociate to the correct, ground state products. This is a well-known[50,51] problem with CASSCF calculations involving the late transition metals, and is due to there being more possible states (and hence more correlation) arising from d^{n-1} s^1 configurations than d^n. For Ni^+, this favors formation of the $3d^8$ 4s (^{4}F) first excited state rather than the $3d^9$ (^{2}D) ground state. The solution is to add additional d orbitals on the metal (typically called the d' space) to the active space, and in this case a complete set of five d orbitals was required. The CASSCF active space then consists of 13 electrons in 14 orbitals. For each symmetry, all quartet states correlating to Ni^+ (^{4}F) and Ni^+ (^{2}D) + S (^{3}P) were averaged. This corresponds to three Σ^+, five Δ and one Γ state (a_1 symmetry); six Π and three Φ states (b_1 or b_2); and three Σ^-, five Δ and one Γ state (a_2 symmetry). The resulting CASSCF potentials then dissociate to the correct asymptotes. For the MRCI, the active space is expanded to also allow promotions from the 3s orbitals on sulfur. In addition, 12 excited states are calculated to ensure that the 9 lowest states are included. Unfortunately, the larger CASSCF active space leads to a prohibitively large icMRCI calculation. In order to make the icMRCI calculation tractable, a subset of the configuration state functions (CSFs) with norm >0.04 were selected, typically leading to ~200 CSFs and ~1.6 x 10^7 configurations in the icMRCI.

In order to assess whether there are low-lying doublet or sextet states, calculations on those states were also carried out at the MRCI+Q/aug-cc-pVQZ level. The lowest sextet state lies >10000 cm^{-1} above the lowest quartet states, so they were not considered further. The lowest doublet state is the $^2\Pi$, which is predicted to lie ~1500 cm^{-1} above the lowest quartet states. Spin-

orbit calculations which simultaneously included the low energy $^4\Sigma^-$, $^4\Delta$ and $^2\Pi$ states were also carried out (without the d' space) using *MOLPRO*, using the MRCI wavefunctions and the Breit-Pauli spin-orbit operator for internal configurations and a mean-field one-electron Fock operator for external configurations.[48,49]

III. Results and Discussion

A. NiO^+

1. Electronic Structure Calculations on NiO^+. The ground state of NiO^+ was determined to be $^4\Sigma^-$ by Nakao et al. in 2001[11] using B3LYP and MRCI calculations. This was confirmed by a wider range of MRCI calculations performed by Sakellaris and Mavridis in 2013.[12] Bond dissociation energy (D_0) values calculated in these studies range from 19000 to 21000 cm^{-1}, with the latter group reporting a recommended value of 19200 cm^{-1}.[12] Sakellaris and Mavridis also characterized a wide range of excited electronic states, of several spin multiplicities. There are nine electronic states (Σ^+, Σ^- (2), Π (3), Δ (2), Φ) for each spin multiplicity (doublet and quartet), that correlate to Ni^+ (^{2}D) + O (^{3}P) ground state products. They calculated seven of these states, for each spin. Excited Ni^+ (^{4}F) + O (^{3}P) give rise to twelve states (Σ^+ (2), Σ^-, Π (3), Δ (3), Φ (2), Γ), each of which can have doublet, quartet or sextet spin. Of these, they calculated a doublet, a quartet and four sextet predissociative states and 8 repulsive states. Our calculations focus on the quartet states and include all the states that correlate to Ni^+ (^{2}D, ^{4}F) + O (^{3}P). These are the most relevant states for optical spectroscopy, but do not include some states that may contribute to the photodissociation dynamics (e.g. predissociation via intersystem crossing). Figure 1 shows calculated MRCI+Q potentials of the ground $^4\Sigma^-$ state of NiO^+, along with several excited $^4\Sigma^-$ and $^4\Pi$ states. These are states that are optically accessible and have vertical excitation energies below 40000 cm^{-1}. The transition intensity from the X $^4\Sigma^-$ state to each of these states is predicted to be weak ($f \leq 0.003$).

2. Photodissociation Spectrum of NiO^+. The photodissociation spectrum of NiO^+ (Figure S1) over the range of 20350 to 27000 cm^{-1} (492 to 370 nm) shows no obvious fragment onset and little to no structure, gradually increasing from zero to low and constant fragment yield from 20800 to 25000 cm^{-1}. Since an onset to form ground state Ni^+ products was not observed, measurements

of the spectrum were extended to energies above the Ni^+ (^4F) threshold in hope of detecting a significant increase in fragment yield which might mark the opening of the higher energy product channel. In this region of the spectrum (27000 to 29200 cm^{-1}), photofragment yield increases again starting at 27700 cm^{-1} with a small peak at 27800 cm^{-1}, then continues to increase before it plateaus at 29000 cm^{-1} at approximately the same intensity as the peak at 27800 cm^{-1}. The lack of a sharp onset in the spectrum near the predicted bond dissociation energy and again upon energetic access of a new product channel makes it difficult to precisely determine D_0 (NiO^+) and characterize the excited states from the spectrum alone. However, imaging the photoproducts formed at different photon energies allows us to make a precise D_0 measurement and gives us additional information on the dissociation dynamics.

3. Images of Ni^+ Fragments. Figure 2 shows a photofragment image of Ni^+ from photodissociation of NiO^+ at 27778 cm^{-1}, along with the resulting total kinetic energy release (KER) distribution. There is moderate KER, indicating that only ground electronic state products are formed. The Ni^+ ground electronic state has two spin-orbit levels, with the $^2D_{3/2}$ lying 1507 cm^{-1} above the $^2D_{5/2}$ ground state; for oxygen, the $^3P_1$ and $^3P_0$ are 158 and 227 cm^{-1}, respectively, above the $^3P_2$ ground state.[52] The KER is sufficiently high that the spin-orbit states are not resolved. However, the KER distribution shows that the propensity for $^2D_{3/2}$ products is higher than that for $^2D_{5/2}$ products. The distribution of signal intensity in the image is radially uniform ('isotropic'). This case is the 'midpoint' in the continuum between two limiting cases of image anisotropy, captured by the anisotropy parameter (β). The first case, limiting parallel ($\beta = 2$), describes a direct photodissociation event where the transition dipole moment is oriented parallel to the principal molecular axis of the parent ion and photodissociation is prompt. If the photolysis laser is vertically polarized, this case gives an image with vertical anisotropy (higher signal intensity at the north and south poles). For a linear molecule, this occurs if the change in orbital angular momentum, $\Delta\Lambda$, is zero. The second case, limiting perpendicular ($\beta = -1$), describes a direct photodissociation event where the transition dipole moment is oriented perpendicular to the principal molecular axis. If the photolysis laser is vertically polarized, this gives an image with horizontal anisotropy (higher signal intensity at the equator). This occurs when $\Delta\Lambda = \pm 1$. The 'midpoint' case, isotropic ($\beta = 0$), describes a photodissociation event where the parent ion is equally likely to fall apart in any orientation regardless of the laser polarization. This last case results in an image with no anisotropy and can occur if: (1) the excited molecules survive for several rotational periods before

dissociating; or (2) at a given photolysis energy, the molecules photodissociate via multiple overlapping parallel and perpendicular transitions, whose contributions to the image anisotropy cancel each other out. For NiO^+ photolyzed at 27778 cm^{-1}, the calculations predict that both mechanisms are active. There are parallel transitions to the 2 $^4\Sigma^-$ and 3 $^4\Sigma^-$ states, both of which correlate to excited products and are thus predissociative at this energy. There is also a perpendicular transition to the 3 $^4\Pi$ state, which has a barrier to dissociation, due to an avoided crossing with the 3 $^4\Pi$ state.

Figure S2 (i) shows a Ni^+ photofragment image taken at slightly higher photon energy (29197 cm^{-1}) and its corresponding KER distribution. A new, low KER channel corresponding to dissociation to excited state Ni^+ (^4F_J) products clearly dominates over the ground state channel. The Ni^+ ($^4F_{9/2}$) state lies 8394 cm^{-1} above the $^2D_{5/2}$ ground state, and the J = 7/2, 5/2 and 3/2 spin-orbit levels lie 936, 1722 and 2270 cm^{-1} above the J = 9/2 level, respectively.[52] Taking the ^4F_J energy splitting into account, the KER distribution in Fig. S2 (i) is, further, consistent with exclusive formation of the lowest energy spin-orbit component, Ni^+ ($^4F_{9/2}$). In contrast to the near isotropic image in Figure 2 ($\beta = 0.10$), the image in Figure S2 (i) shows slight parallel anisotropy ($\beta = 0.30$) suggesting photodissociation at 29197 cm^{-1} is more prompt and is due to excitation to a $^4\Sigma^-$ state. Dissociation at progressively higher energies leads to production of the other ^4F_J spin-orbit states. While the kinematics of detecting the heavy Ni^+ fragment in dissociation of NiO^+ are not ideal for maximum resolution and O (^3P_J) spin-orbit states (227 cm^{-1} spread) 'smear' the Ni^+ rings, we are still able to resolve the lowest two spin orbit states (936 cm^{-1} spacing) of the Ni^+ (^4F_J) fragments at a photolysis energy of 30075 cm^{-1} (Figure 3). Ni^+ ($^4F_{9/2}$) fragments account for ~80% of the photoproduct yield, with Ni^+ ($^4F_{7/2}$) making up the remaining 20%. At 30769 cm^{-1} however, with Ni^+ ($^4F_{5/2}$) becoming energetically accessible, individual Ni^+ spin orbit levels are less well resolved (Figure S2, ii). Although the Ni^+ ($^4F_{3/2}$) product channel is energetically accessible by 31646 cm^{-1}, it is highly unfavored relative to each of the lower energy spin-orbit channels (Figure S2, iii). It is apparent from the KER distributions in Figure S2 (ii, iii) that the propensity for Ni^+ ^4F_J spin-orbit state products generally decreases as the energy of the spin orbit state increases. The trend in spin-orbit propensities for Ni^+ (^4F_J) products is opposite that for ^2D_J products. In addition, parallel anisotropy is consistent across all images (Fig. 3, $\beta = 0.30$, inner ring and 1.06, outer ring; Fig. S2 ii) $\beta = 0.31$, inner ring and 1.14, outer ring; Fig. S2 iii) $\beta = 1.65$) collected at photolysis

energies above the Ni^+ (^4F) product threshold, suggesting dissociation over this entire region results from excitation to the same or other nearby $^4\Sigma^-$ state(s). Based on the calculations, this is likely the 3 $^4\Sigma^-$ state, which has a significantly larger bond length than the ground state, so vertical excitation accesses the repulsive inner wall of the potential.

For a given image, subtracting the peak total KER in the KER distribution from the photolysis energy gives a precise value of the product threshold, and upon subtraction of the Ni^+ (^4F) product energy, the NiO^+ bond dissociation energy (D_0). A more accurate approach is to plot photolysis energy (with excited photoproduct energy subtracted) versus total KER for a series of images above the Ni^+ (^4F) threshold and fit the points to a line.[53] The y-intercept of the plot is equal to D_0, as shown in Figure S3. This intercept method gives the most precise measurement of the NiO^+ bond dissociation energy reported to date ($D_0 = 244.6 \pm 2.4$ kJ/mol, 20450 ± 200 cm^{-1}). Table 1 compiles all experimentally measured values and selected theoretical values of D_0 (NiO^+). Our VMI measured D_0 agrees with the later, less precise guided ion beam measurement by Armentrout and coworkers,[16] but not with their earlier, more precise measurement.[15] The most sophisticated ab initio calculations, at the MRCI level and with scalar relativistic effects using the second-order Douglas-Kroll-Hess (DKH2) approximation, are very close to our measured value, as is the averaged coupled pair functional (ACPF) result.[12] Near the measured D_0, the photodissociation spectrum shows zero fragment yield, suggesting NiO^+ does not absorb at D_0, or that the fluorescence lifetime is shorter than the photodissociation lifetime. Lack of absorption at this photon energy is consistent with calculations by Sakellaris and Mavridis, which predict the two closest excited states to the Ni^+ (^2D_J) product threshold to be the 1 $^4\Gamma$ ($T_e = 15504$ cm^{-1}) and 1 $^6\Delta$ ($T_e = 22107$ cm^{-1}) states, neither to which are optically allowed transitions from the $^4\Sigma^-$ ground state, and our calculations, which predict that there are few excited states with allowed electronic transitions near the dissociation threshold, and transitions to those states are weak.

B. NiS^+

1. Electronic Structure Calculations on NiS^+. Although NiS^+ and NiO^+ are isoelectronic, the relative energies of their electronic states are quite different. The $^4\Delta$ state, which lies[12] ~6000 cm^{-1} above the $^4\Sigma^-$ ground state in NiO^+, is predicted to be the ground state in NiS^+ with the $^4\Sigma^-$ lying only ~200 cm^{-1} higher in energy at the B3LYP[13] and CCSD(T)[14] level. Our calculations, at the MRCI+Q/aug-cc-pVQZ level, predict that the $^4\Delta$ lies 627 cm^{-1} above the $^4\Sigma^-$. Figure 4 shows

the potentials for all quartet states of NiS^+ that correlate to Ni^+ (^2D, ^4F) + S. In this figure, $^4\Sigma^-$ and $^4\Delta$ states are highlighted, as they are accessible by parallel transitions from the 1 $^4\Sigma^-$ and 1 $^4\Delta$ states. Table S1 gives spectroscopic parameters for all of these states, while Figures S5 and S6 show selected excited states.

Spin-orbit coupling will preferentially stabilize the lowest lying spin-orbit levels of the $^4\Delta$ state relative to the $^4\Sigma^-$ state. In order to quantify this effect, we carried out spin-orbit calculations, including the three lowest-lying electronic states: the $^4\Delta$, $^4\Sigma^-$ and $^2\Pi$ states. These calculations were done using the standard (not expanded) d space for Ni, as including the d' space in the spin-orbit calculations is prohibitively expensive. Also, the inclusion of the d' space has only a small effect on the potentials near equilibrium. The results are shown in Figure S7. With this active space, the ground state is $^4\Sigma^-$, with the $^4\Delta$ and $^2\Pi$ states 403 and 838 cm^{-1} higher in energy, respectively. Including spin-orbit splitting, the ground state is $^4\Delta_{7/2}$. The $^4\Delta_\Omega$ (Ω = 5/2, 3/2, 1/2) states are at 454, 846, and 1655 cm^{-1}, respectively. To first order, Σ states do not have spin-orbit splitting, but they can have second-order spin orbit splitting, which is typically much smaller. The $^4\Sigma^-_{3/2}$ state is at 26 cm^{-1} and the $^4\Sigma^-_{1/2}$ is at 66 cm^{-1}; the $^2\Pi_{3/2}$ is at 724 cm^{-1} and the $^2\Pi_{1/2}$ is at 1542 cm^{-1}. So, including spin-orbit interactions stabilizes the $^4\Delta_{7/2}$ and $^2\Pi_{3/2}$ states by 429 and 140 cm^{-1}, respectively, relative to the $^4\Sigma^-_{3/2}$ state. Combining this shift with the energies calculated using the expanded d space, the calculations predict that the $^4\Sigma^-_{3/2}$ is the ground state, only 198 cm^{-1} below the $^4\Delta_{7/2}$. This difference is smaller than the relative accuracy of the calculations, which thus do not clearly indicate whether $^4\Delta$ or the $^4\Sigma^-$ is the true ground state. So, in the subsequent discussion we will consider optically allowed transitions from the $^4\Delta_{7/2}$, $^4\Sigma^-_{3/2}$ and $^4\Sigma^-_{1/2}$ states, as they may be populated at the temperature of the ion trap.

2. Photodissociation Spectrum of NiS^+. The photofragment spectrum of NiS^+ was measured by our group previously on a separate instrument,[13] with ions formed by laser ablation and cooled by supersonic expansion. In this work, a segment of the spectrum was re-measured with ions cooled in a 3D quadrupole trap[41] at several trap temperatures with He or D_2 buffer gas. No dissociation is observed below ~20000 cm^{-1} and the spectra contain several peaks, with rich sub-structure (Figure 5). A few peaks change in intensity as the trap is cooled. One example is the lowest energy peak in the spectrum (labeled 1*, at 20022 cm^{-1}), which loses approximately half its

intensity as the trap is cooled from 291 (red) to 80 K (blue). The reduced intensity suggests this peak arises from photodissociation of parent ions that are vibrationally excited or in a low-lying excited electronic or spin-orbit state rather than the ground state. Another example is the peak at 20164 cm^{-1} (labeled 3), which increases in intensity by approximately two-fold from 291 K to 80 K. The gain in intensity suggests that peak 3 originates from the ground state of NiS^+. Although most of the remaining peaks in the spectrum become narrower and sharper as the trap is cooled, they do not change significantly in intensity.

3. Images of Ni^+ Fragments. Photofragment images were taken at several peaks in the spectrum to determine D_0 (NiS^+) and to determine the origin of the three lowest energy peaks in the spectrum (1, 2 and 3). The ground state of sulfur is $^3P_2$, with the $^3P_1$ and $^3P_0$ states at 396 and 574 cm^{-1}, respectively.[52] The larger spin-orbit splitting of sulfur relative to oxygen and improved kinematics of NiS^+ relative to NiO^+ mean that the spin-orbit states of both fragments can be resolved near threshold. Figure 6 shows a photofragment image at 20631 cm^{-1} (peak 4 in Figure 5). The resulting KER distribution has two distinct peaks spaced by ~400 cm^{-1}, consistent with formation of ground state Ni^+ ($^2D_{5/2}$) and both ground state S ($^3P_2$) (higher KER) and first excited spin-orbit state S ($^3P_1$) (lower KER) products. Both the lower and higher KER channels have slightly parallel fragment distribution (β = 0.29 and 0.28, respectively). This distribution is consistent with a parallel electronic transition where dissociation to S ($^3P_1$) products competes with dissociation to the S ($^3P_2$) channel, with a product branching ratio of 3:2. At 21706 cm^{-1} (peak 5 in Figure 5), Ni^+ ($^2D_{5/2}$) + S ($^3P_{0,1,2}$) products are all formed (70%) and compete with Ni^+ ($^2D_{3/2}$) + S ($^3P_2$) (30%) as shown in Figure 7. The higher KER channel corresponding to Ni^+ ($^2D_{5/2}$) has slight parallel anisotropy (β = 0.43), while the lower KER channel is isotropic (β = 0.08).

A photofragment image at 20164 cm^{-1} (peak 3) shows only formation of Ni^+ ($^2D_{5/2}$) + S ($^3P_2$), with low KER, and gives a dissociation energy that is consistent with those from the higher-energy peaks. However, images at 20022 and 20103 cm^{-1} (peaks 1* and 2*) give significantly lower D_0, indicating that they arise from hot ions. Based on the KER distributions, and assuming ground state products, peaks 1* and 2* are due to ions with an internal energy of 166 ± 50 cm^{-1} and 81 ± 30 cm^{-1}, respectively. We therefore assign peaks including and to the blue of peak 3 as originating from ground state ($1\ ^4\Delta$ or $1\ ^4\Sigma^-$) NiS^+. The fundamental vibrational frequencies of the $1\ ^4\Delta$ and $1\ ^4\Sigma^-$ states are calculated to be ν_0 = 417 and 413 cm^{-1}, respectively (Table S1), so peaks

1* and 2* are not due to vibrational hot bands. Rather, peaks 1* and 2* likely originate from higher lying spin-orbit levels of the low-lying $^4\Delta$ and $^4\Sigma^-$ states. As argued below, we assign the ground level as $^4\Delta_{7/2}$ and the hot bands as originating from the $^4\Sigma_{3/2}$ and $^4\Sigma_{1/2}$ levels.

The dissociation energy of NiS^+ is determined by plotting photolysis energy versus total KER for production of ground state products determined at several photolysis energies and fitting the points to a line. The results, shown in Figure S4**,** give D_0 (NiS^+) = 240.3 ± 1.4 kJ/mol, 20090 ± 120 cm^{-1}). Experimentally measured and selected theoretical values of D_0 (NiS^+) are shown in Table 2. Rue et al.[17] measured the bond strength using the endothermic reaction of Ni^+ with OCS in a guided ion beam instrument. Hettich et al.[31] measured the photodissociation of NiS^+ in an ICR, using a lamp/monochromator with 10 nm resolution, and assuming that the dissociation onset occurs at the bond dissociation energy. Our previous study,[13] using laser photodissociation, determined the onset with much higher precision but was still limited by uncertainty in whether small peaks near the dissociation onset are due to hot ions. Our VMI measurement of D_0 (NiS^+) agrees with all of the previous values but has higher precision. Calculations by Lakunza et al.[14] at the CCSD(T)/TZVP++G(3df,2p)//B3LYP level (D_0 (NiS^+) = 234 kJ/mol) and, in this work, at the MRCI+Q/aug-cc-pVQZ level (235 kJ/mol) are nearly identical and quite close to the measured value, underestimating the bond strength by 5-6 kJ/mol. The present study confirms that dissociation occurs at the thermodynamic onset, and determines that the first two, small, peaks in the spectrum are from hot ions. Thus, even when dissociation occurs at the thermodynamic onset, imaging is a valuable complement to spectroscopy. Our measurement of D_0 (NiS^+) also refines the ionization energy of NiS. Matthew et al.[54] recently measured the dissociation energy of the neutral with very high precision: D_0 (NiS)=3.651 ± 0.003 eV. Combining this value with our measurement of D_0 (NiS^+) and IE (Ni), we obtain a more precise estimate of IE (NiS) = 8.80 ± 0.02 eV (849 ± 1.7 kJ/mol).

The MRCI+Q calculations, in conjunction with the images, help to assign the photodissociation spectrum. The fragment anisotropy in the images ranges from parallel to isotropic. Also, as shown in Table S1, the calculated oscillator strengths for perpendicular transitions are much smaller than for parallel transitions. Thus, we assign the majority of the spectrum to be due to parallel transitions, $^4\Sigma^- \leftarrow {}^4\Sigma^-$ or $^4\Delta \leftarrow {}^4\Delta$. The only $^4\Sigma^-$ state in the relevant energy region is the 3 $^4\Sigma^-$ state, shown in blue, bold in Figure 4. This state has calculated T_0 = 19006 cm^{-1}, a vertical transition energy of 21382 cm^{-1}, a vibrational frequency of ω_e = 314 cm^{-1},

and integrated oscillator strength of $f = 0.0103$. Experimentally, the dissociation yield for NiS^+ is significantly higher than for NiO^+ and is consistent with an integrated oscillator strength of this magnitude. A simulated absorption spectrum due to this transition ($3\ ^4\Sigma^- \leftarrow 1\ ^4\Sigma^-$) is shown in the dashed blue trace at the bottom of Figure 5. This simulated spectrum is far less complex than is experimentally observed. If second-order spin-orbit splitting is included, the propensity is for $^4\Sigma^-_{3/2} \leftarrow {}^4\Sigma^-_{3/2}$ and $^4\Sigma^-_{1/2} \leftarrow {}^4\Sigma^-_{1/2}$ transitions rather than $^4\Sigma^-_{1/2} \leftarrow {}^4\Sigma^-_{3/2}$ and $^4\Sigma^-_{3/2} \leftarrow {}^4\Sigma^-_{1/2}$. This would lead to a series of doublets whose relative intensities would depend on the temperature of the ion trap, which is not observed in the experiment, so it is unlikely that the observed spectrum is solely due to transitions from a $^4\Sigma^-$ state. There are three $^4\Delta$ states in the energy region of interest, the 3, 4 and 5 $^4\Delta$, shown in green, bold in Figure 4. These states have several avoided crossings at energies near 20000 cm^{-1} and the resulting potentials are anharmonic. Transitions to all three from the $1\ ^4\Delta$ are predicted to be fairly intense, with $f = 0.0088$ for $3\ ^4\Delta$ and 0.0132 and 0.0079 for the 4 and 5 $^4\Delta$. The simulated spectra, shown in the green dashed traces at the bottom of Figure 5, are quite complex, as they contain contributions from all three states at low energy, and then simplify somewhat above ~21500 cm^{-1} when contributions from the 4 and 5 $^4\Delta$ dominate. Simulated spectra due to the $3\ ^4\Sigma^- \leftarrow 1\ ^4\Sigma^-$ and $3, 4, 5\ ^4\Delta \leftarrow 1\ ^4\Delta$ transitions were summed to give the total simulated spectrum, shown in the red dashed trace at the bottom of Figure 5. Intensities in the total spectrum were multiplied by 3 for easier visualization. Some (but not all) of the multiplet structure in the first five features of the experimental spectrum (20000 – 21200 cm^{-1}) is captured by the simulation, with triplets or doublets (depending on the simulated Gaussian width) predicted to arise from the $3\ ^4\Sigma^- \leftarrow 1\ ^4\Sigma^-$ and $4, 5\ ^4\Delta \leftarrow 1\ ^4\Delta$ transitions. The remaining seven features in the experimental spectrum are clear doublets, a motif which is well-modeled by the simulation, which indicates they are due to transitions to the 4 and 5 $^4\Delta$ states. The relative intensities of peaks in the simulated doublet and triplet features do not precisely match experimental intensities. However, the three $^4\Delta$ states all lie at similar energies and interact, making it challenging to accurately calculate their relative intensities and energies. We therefore assign the bulk of the spectrum to $4\ ^4\Delta \leftarrow 1\ ^4\Delta$ and $5\ ^4\Delta \leftarrow 1\ ^4\Delta$ vibronic transitions, with perhaps some contribution from the $3\ ^4\Sigma^- \leftarrow 1\ ^4\Sigma^-$ transition below 20700 cm^{-1}. We also assign hot band peaks 1* and 2* to transitions to the $3\ ^4\Sigma^-$ state from the $1\ ^4\Sigma_{1/2}^-$ and $1\ ^4\Sigma_{3/2}^-$ states, respectively, based on varied temperature spectra and KER

distributions of images taken at the corresponding photon energies. This implies that the 1 $^4\Sigma_{1/2}^-$ and 1 $^4\Sigma_{3/2}^-$ states lie 166 ± 50 and 81 ± 30 cm^{-1} respectively above the 1 $^4\Delta_{7/2}$ ground state.

It is useful to compare the electronic states of NiS^+ with isoelectronic CoS, which has been studied more extensively by experiment and theory. Although an early atom superposition and electron delocalization molecular orbital (ASED-MO) theory calculation[55] on CoS assumed a $^4\Sigma^-$ ground state, subsequent studies by Bauschlicher and Maitre[56] at the CCSD(T) and ACPF level correctly predict a $^4\Delta$ ground state, and a DFT study by Bridgeman and Rothery[57] predicts that the $^4\Sigma^-$ lies 1770 cm^{-1} above the $^4\Delta$. Ziurys and coworkers[58] measured the microwave spectrum of CoS and determined the ground state to be $^4\Delta_{7/2}$, with r_0 = 1.97798506 Å. An infrared emission study by Bernath and coworkers characterized the low-lying $^4\Phi$ (T_0 = 3409 cm^{-1}) and $^4\Pi$ (T_0 = 5620 cm^{-1}) states.[59] As part of a series of studies[60–62] on CoS, Chen and coworkers measured the laser-induced fluorescence spectrum[60] of jet-cooled CoS from 15200 to 19000 cm^{-1}. They observed 57 vibronic bands and assigned them to five different electronic transitions. Four of these are transitions to different $^4\Delta_{7/2}$ states and one is a transition to a $^4\Pi_{5/2}$, all from the $^4\Delta_{7/2}$ ground state. This analysis of the CoS LIF spectrum from 15200 to 19000 cm^{-1} echoes our assignment of three separate $^4\Delta \leftarrow 1\ ^4\Delta$ transitions in the NiS^+ photodissociation spectrum from 19900 to 23200 cm^{-1}.

C. Comparison of Bonding in MO^+ and MS^+

Figure 8 and Table 3 compare the M^+-O and M^+-S bond strengths for the 3d transition metals. The early transition metal cations form extremely strong bonds to oxygen, and much weaker bonds to sulfur. The late transition metals form much weaker bonds to oxygen, and, for each metal, the M^+-O and M^+-S bond dissociation energies are similar. This trend in bonding, and its dependence on the occupied molecular orbitals has been discussed in detail for the cations,[12,30,63,64] and neutrals[56,57,65] and will be reviewed here. For some molecules, there is substantial multi-configurational character, so this description is only approximate. The valence molecular orbitals of the transition metal oxides and sulfides primarily arise from the 3d and 4s orbitals on the metal and the oxygen 2s and 2p, or sulfur 3s and 3p. These lead to four σ, two pairs of π and one pair of δ molecular orbitals. The orbitals for NiO^+ and NiS^+ are shown in Figure S8. These orbitals will first be described for MO^+, then similarities and differences between the oxides

and sulfides will be discussed. The non-bonding 1σ is almost entirely 2s on oxygen. The 2σ is a bonding combination of $3d\sigma$ ($3d_{z^2}$) on the metal and $2p_z$ on oxygen. The $1\pi_x$ and $1\pi_y$ are bonding combinations of metal $3d\pi$ ($3d_{xz}$ and $3d_{yz}$) and oxygen $2p_x$ and $2p_y$. For ScO^+ there are 8 valence electrons, so these four orbitals are filled, leading to a strong Sc^+-O bond. In TiO^+ and VO^+ the additional electrons populate the non-bonding $1\delta_+$ and $1\delta_-$ orbitals and are unpaired. These orbitals are the metal $3d\delta$ ($3d_{xy}$ and $3d_{x^2-y^2}$). For CrO^+ and MnO^+, rather than add electrons to the 1δ to form low-spin states, they are unpaired and go into the anti-bonding 3σ and 2π orbitals, respectively.[64] As a result, the Cr^+-O bond is significantly weaker than in the earlier metals, and the Mn^+-O bond is weaker still. High spin is again favored for FeO^+, whose $^6\Sigma^+$ ground state has unpaired electrons in the $1\delta_+$, $1\delta_-$, $2\pi_x$, $2\pi_y$ and 3σ. In CoO^+ and NiO^+ the additional electrons go into the 1δ orbitals, so FeO^+, CoO^+ and NiO^+ have similar bond strengths. CuO^+ has a significantly weaker bond, as the 3σ is now doubly occupied. In ZnO^+ the next electron goes into the 2π. The reduced covalency means that the bonding in CuX^+ and ZnX^+ (X = O, S) can be viewed as largely electrostatic in nature, which leads to similar bond strengths for CuX^+ and ZnX^+, and for larger bond strengths for the sulfides than the oxides, due to the greater polarizability of sulfur.[30]

Although the orbitals in MO^+ and MS^+ are similar, there are important differences. Compared to those in MO^+, the bonding orbitals in MS^+ have less bonding character and the antibonding orbitals have less antibonding character. The 1π in MS^+ is less strongly bonding, which helps to explain why the M^+-S bond strengths are ~200 kJ/mol lower than those of M^+-O for M=Sc, Ti, V. Concomitantly, the 2π has much less electron density on the metal and is thus much less strongly antibonding. So, occupying the 2π reduces the M^+-S bond strength, but to a much lesser extent than for the oxides. Also, the 3σ in MS^+ is nearly completely metal $3d_{z^2}$ and is non-bonding, rather than anti-bonding. So, there is little reduction in the M^+-S bond strength as this orbital is occupied. This observation underlies a key difference between the electronic structures of NiO^+ and NiS^+. In NiS^+ calculations predict that the $^4\Sigma^-$ and $^4\Delta$ are nearly degenerate and have very similar bond lengths and vibrational frequencies. The dominant electron configuration for the $^4\Sigma^-$ state is $1\sigma^2\ 2\sigma^2\ 1\pi_x^2\ 1\pi_y^2\ 1\delta_+^2\ 1\delta_-^2\ 2\pi_x^1\ 2\pi_y^1\ 3\sigma^1$ (MRCI coefficient of 0.82), while for the $^4\Delta$ state it is $1\sigma^2\ 2\sigma^2\ 1\pi_x^2\ 1\pi_y^2\ 1\delta_+^2\ 1\delta_-^1\ 2\pi_x^1\ 2\pi_y^1\ 3\sigma^2$ (MRCI coefficient of 0.79). Thus, there is little difference in energetics or bonding between having an extra electron in

the 1δ or 3σ orbital. The situation is quite different for NiO^+. The ground state is clearly $^4\Sigma^-$, with the $^4\Delta$ state 5600 cm^{-1} higher in energy at the MRCI+Q level.[12] In addition, the $^4\Delta$ state has a substantially longer bond (1.708 Å vs. 1.588 Å) and lower vibrational frequency than the $^4\Sigma^-$ state.[12] So, the 3σ is clearly anti-bonding and at higher energy than the 1δ. The differences in the composition and relative energies of the 3σ and 1δ orbitals in NiO^+ and NiS^+ help to explain the observed differences between the ions' electronic structures.

IV. Conclusions

We find the bond strengths of NiO^+ (D_0 = 244.6 ± 2.4 kJ/mol) and NiS^+ (D_0 = 240.3 ± 1.4 kJ/mol) are very close to each other; previous reports indicated a larger difference, overestimating D_0 (NiO^+). The proximity of the bond energies is likely due to a cancelling out of the effects of contributions from strongly bonding and strongly antibonding occupied orbitals in NiO^+ versus weakly bonding and weakly antibonding occupied orbitals in NiS^+. The photodissociation spectrum of NiO^+ from 20350 to 29200 cm^{-1} is weak, very broad and provides little information, consistent with the lack of optically accessible excited electronic states near D_0 and the relatively low oscillator strength of transitions to accessible states near the Ni^+ (^4F) threshold. The spectrum of NiS^+ from 19900 to 23200 cm^{-1} exhibits a clear vibrational progression of ~280 cm^{-1} with complex sub-structure. The observed features are mostly due to two overlapping electronic transitions, from the X $^4\Delta_{7/2}$ ground state to the 4 $^4\Delta_{7/2}$ and 5 $^4\Delta_{7/2}$ states. The 3 $^4\Delta \leftarrow$ 1 $^4\Delta$ and 3 $^4\Sigma^- \leftarrow$ 1 $^4\Sigma^-$ transitions may also contribute to some of the lower energy features below 20700 cm^{-1}. The near-degeneracy of the 1 $^4\Sigma^-$ and 1 $^4\Delta$ states of NiS^+, which in NiO^+ are separated by 5600 cm^{-1}, is explained by the near energetic equivalence of the 3σ and 1δ orbitals. Two peaks in the NiS^+ spectrum have been assigned to hot bands likely originating from the 1 $^4\Sigma_{3/2}^-$ and 1 $^4\Sigma_{1/2}^-$ states as determined from temperature dependent spectra and confirmed by images of the Ni^+ photofragments on each of the suspected 'hot' peaks. NiO^+ photofragment images indicate that below the Ni^+ (^4F_J) threshold, at 27778 cm^{-1}, NiO^+ photodissociates to form Ni^+ (^2D_J) products in both spin-orbit levels, with higher-energy J = 3/2 products favored over J = 5/2. Above the Ni^+ (^4F_J) threshold, $^4F_{9/2}$ products dominate with each new spin-orbit level becoming less favored as it becomes energetically accessible. The Ni^+ (^4F_J) dissociation channels show vertical anisotropy, indicating rapid dissociation via a parallel transition, most likely the 3 $^4\Sigma^- \leftarrow$ X $^4\Sigma^-$. Only Ni^+ (^2D_J)

+ S (^3P_J) products are accessible at photon energies in the range of the NiS^+ spectrum, but the spin-orbit states of Ni^+ and S products are resolved in the images. We find that the first excited spin-orbit state of sulfur ($^3P_1$) is slightly favored over the ground spin-orbit state ($^3P_2$) in dissociation to Ni^+ ($^2D_{5/2}$) + S ($^3P_{1,2}$). The propensities for the first two Ni^+ spin-orbit states show the opposite trend, with lower energy Ni^+ ($^2D_{5/2}$) + S (^3P_J) products slightly favored over Ni^+ ($^2D_{3/2}$) + S ($^3P_2$) products. The latter trend is also the reverse of that observed in dissociation of NiO^+ to Ni^+ ($^2D_{5/2, 3/2}$) + O (^3P_J).

Supporting Information Available

Full reference 48; all quartet electronic states of NiS^+ correlating to ground state and first excited state products (Table S1); photodissociation spectrum of NiO^+ (Figure S1); additional NiO^+ photofragment images (Figure S2); plots for determination of D_0 (NiO^+) and D_0 (NiS^+) by the y-intercept method (Figures S3 and S4, respectively); potential energy curves for the $^4\Sigma^-$, $^4\Delta$, and $^4\Gamma$ states (Figure S5) and the $^4\Pi$ and $^4\Phi$ states (Figure S6) of NiS^+; potential energy curves for spin-orbit states of the three lowest-lying electronic states of NiS^+ (Figure S7); molecular orbital diagrams for the 1 $^4\Sigma^-$ states of NiO^+ and NiS^+ (Figure S8).

Acknowledgement

Financial support from the National Science Foundation under award no. CHE-1856490 is gratefully acknowledged. The MOLPRO calculations were carried out at the National Energy Research Scientific Computing Center, a DOE Office of Science User Facility supported by the Office of Science of the U.S. Department of Energy under Contract No. DE-AC02-05CH11231.

Tables and Figures

Table 1. Experimental and Theoretical Ground State Bond Dissociation Energies (D_0) of NiO^+ ($^4\Sigma^-$).

Species	D_0 (kJ/mol)	Experiment
NiO^+	260.7 ± 6.6	ion beam[15]
	254 ± 19	ion beam[16]
	244.6 ± 2.4	VMI (present study)
		Theory
NiO^+	249	MRCI-L+DKH2+Q[12]
	239	MRCI+DKH2+Q[12]
	241	ACPF+DKH2[12]
	228	MR-SDCI[11]
	225	B3LYP[18]

Table 2. Experimental and Theoretical Ground State Bond Dissociation Energies (D_0) of NiS^+.

Species	D_0 (kJ/mol)	Experiment
NiS^+	251 ± 21	photodissociation[31]
	≤ 238 ± 4	photodissociation[13]
	237 ± 4	ion beam[17]
	240.3 ± 1.4	VMI (this work)
		Theory
NiS^+	225	B3LYP[13]
	232	B3LYP[14]
	234	CCSD(T)//B3LYP[14]
	235	MRCI+Q (this work)

Table 3. Experimental Bond Dissociation Energies of MO^+ and MS^+.

M^+ Species	D_0 (MO^+) (kJ/mol)	Ref. for MO^+	D_0 (MS^+) (kJ/mol)	Ref. for MS^+
Sc^+	689 ± 5	[22]	480 ± 5	[28]
Ti^+	664 ± 7	[21]	457 ± 7	[28]
V^+	584.0 ± 0.2	[26]	359 ± 9	[27]
Cr^+	357 ± 5	[19]	259 ± 16	[29]
Mn^+	242 ± 5	[25]	243 ± 23	[29]
Fe^+	339.6 ± 2	[23]	297 ± 4	[30]
Co^+	320 ± 6	[15]	285 ± 9	[30]
Ni^+	244.6 ± 2.4	this work	240.3 ± 1.4	this work
Cu^+	131.2 ± 4	[24]	200 ± 14	[17]
Zn^+	161 ± 5	[20]	198 ± 12	[17]

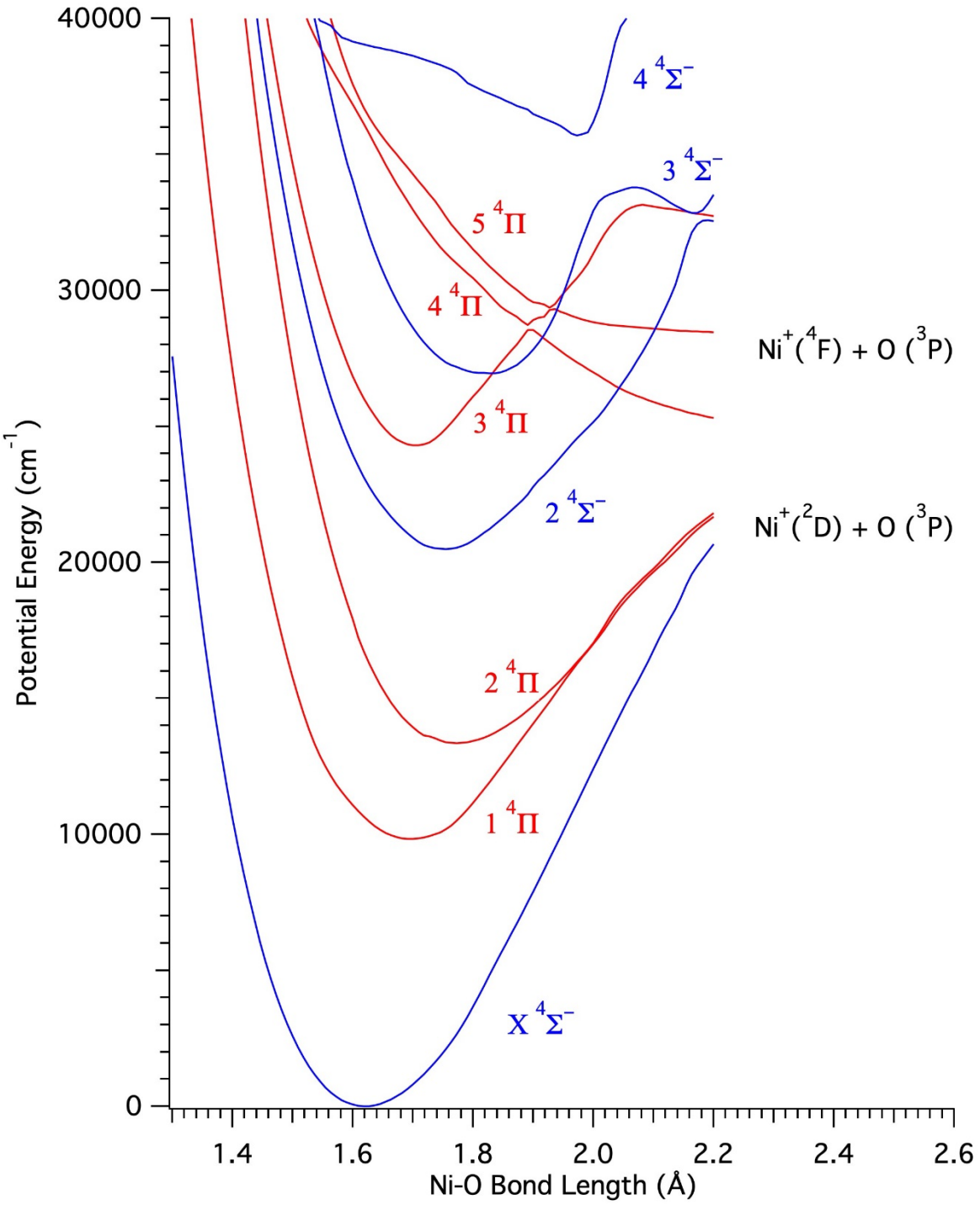

Figure 1. Potential energy curves for $^4\Sigma^-$ and $^4\Pi$ electronic states of NiO^+ with vertical excitation energies below 40000 cm^{-1} calculated at the MRCI+Q/aug-cc-pVQZ level.

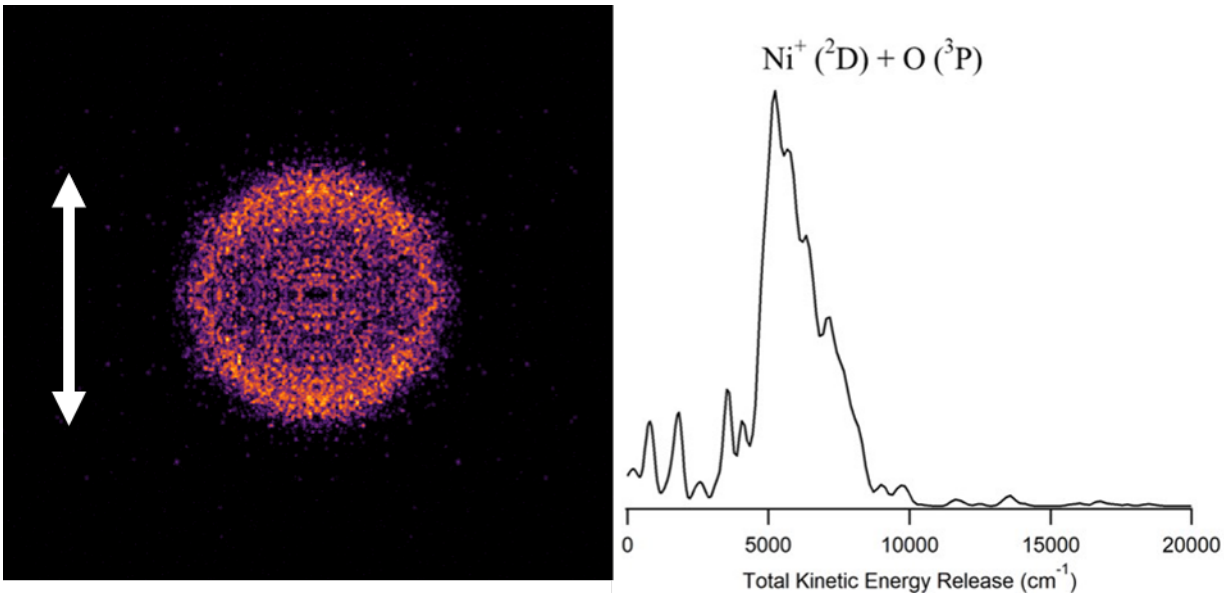

Figure 2. Photofragment image of Ni^+ made by dissociating NiO^+ at 27778 cm^{-1} and the corresponding velocity distribution converted to total kinetic energy release. All NiO^+ images were collected with the ion trap at 55 K and with He buffer gas. The image shown has been top/bottom and left/right symmetrized. Laser polarization is vertical (white arrow).

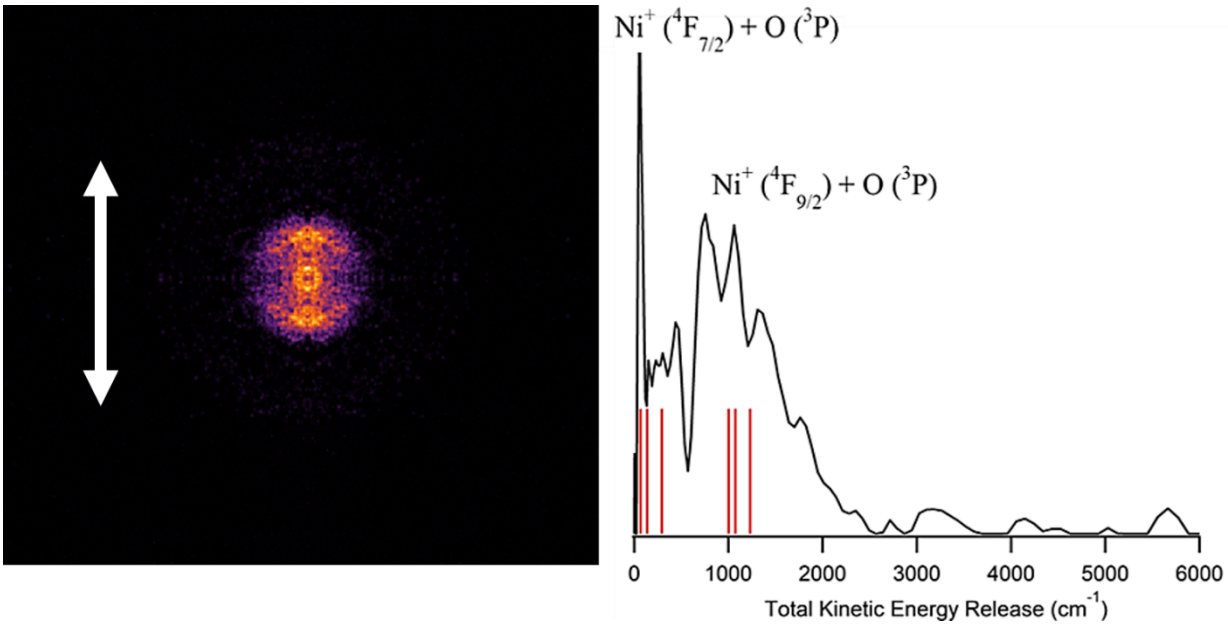

Figure 3. Photofragment image of Ni^+ made by dissociating NiO^+ at 30075 cm^{-1} and the corresponding velocity distribution converted to total kinetic energy release. The image shown has been top/bottom and left/right symmetrized. Laser polarization is vertical (white arrow). Product state reference points along the TKER axis (red vertical lines) are calculated by subtracting the measured D_0 (20450 cm^{-1}) and individual product state energies from the photolysis energy. Groups of three lines reference Ni^+ spin-orbit states, while single lines within a group reference O atom spin-orbit states. Reference points are not absolute assignments, as O atom spin-orbit states are not resolved.

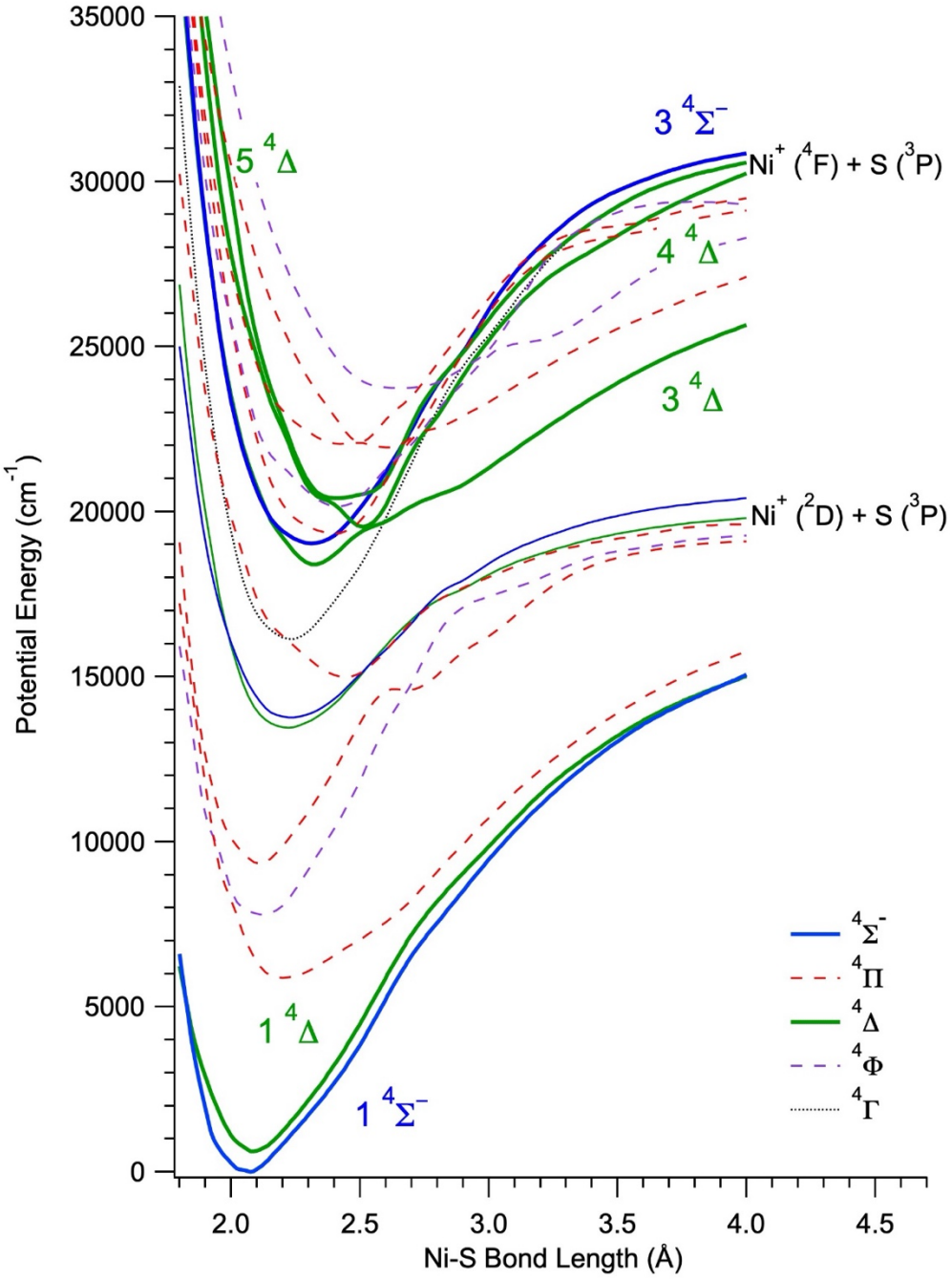

Figure 4. Potential energy curves for $^4\Sigma^-$, $^4\Pi$, $^4\Delta$, $^4\Phi$, and $^4\Gamma$ states of NiS^+ that correlate to ground and first excited state products calculated at the MRCI+Q/aug-cc-pVQZ level. Calculations use the expanded d space in the MCSCF.

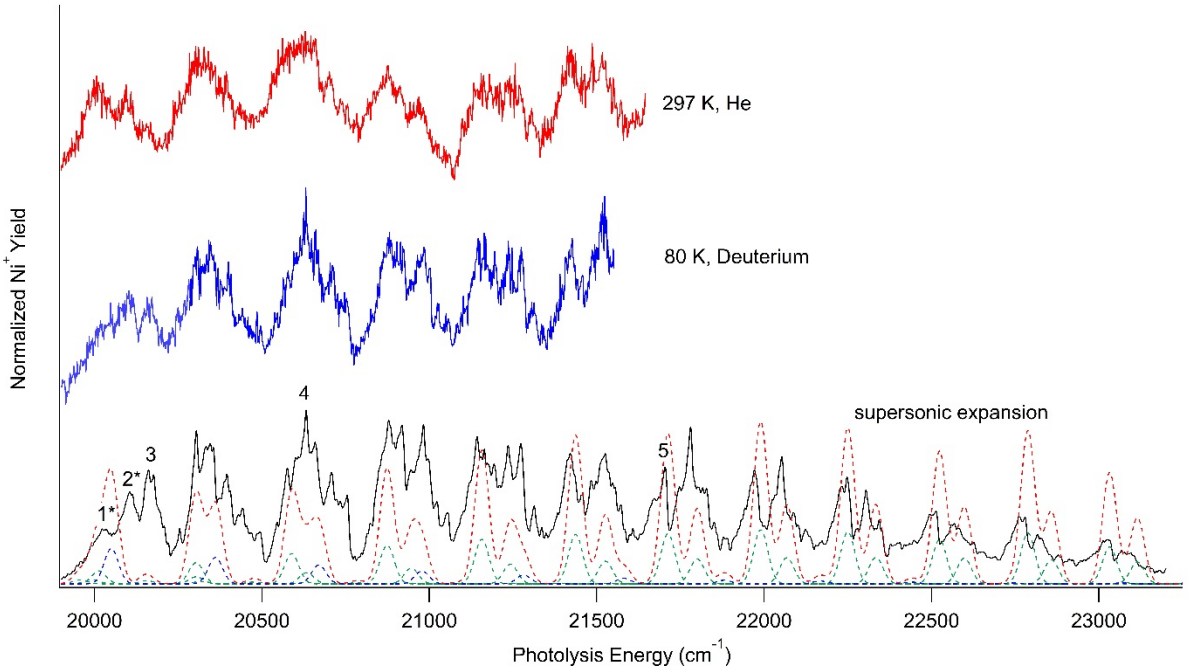

Figure 5. Photodissociation spectrum of NiS^+ near the Ni^+ (^2D) photofragment threshold under various conditions: supersonic expansion[13] (black solid); thermalized in a 3D quadrupole ion trap at 80 K with deuterium buffer gas (blue solid); thermalized in the ion trap at 291 K with helium buffer gas (red solid). Total simulated spectrum (red dash) and individual contributions from $\Sigma \leftarrow \Sigma$ and $\Delta \leftarrow \Delta$ transitions (blue and green dash, respectively) shifted by 2130 cm^{-1} to lower energy are shown at the bottom. The simulations use a 50 cm^{-1} FWHM Gaussian. Intensities in the total simulated spectrum are multiplied by 3 for easier visualization. 1* and 2* labels denote suspected spin-orbit hot bands, and 3 denotes the lowest energy peak assigned to a transition originating from the ground state.

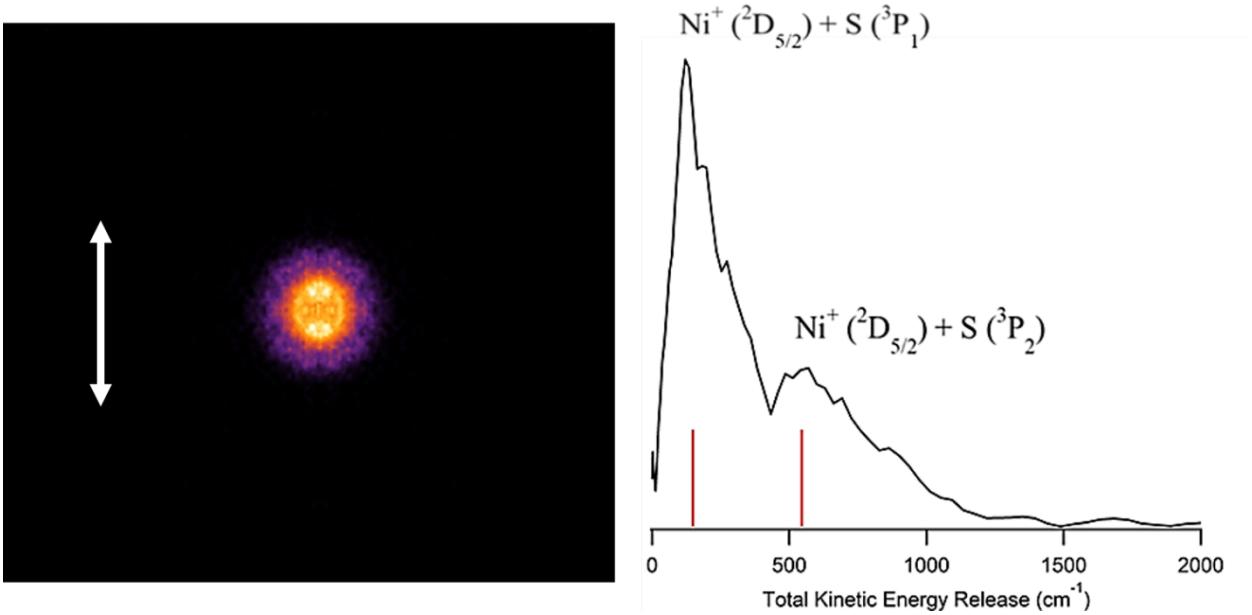

Figure 6. Photofragment image of Ni^+ made by dissociating NiS^+ at 20631 cm^{-1} and the corresponding velocity distribution converted to total kinetic energy release. All NiS^+ images were collected with the ion trap at 80 K and with D_2 buffer gas. The image shown has been top/bottom and left/right symmetrized. Laser polarization is vertical (white arrow). Product state reference points along the TKER axis (red vertical lines) are calculated by subtracting the measured D_0 (20090 cm^{-1}) and individual product state energies from the photolysis energy. Since S atom spin-orbit states are resolved, reference points also serve as assignments.

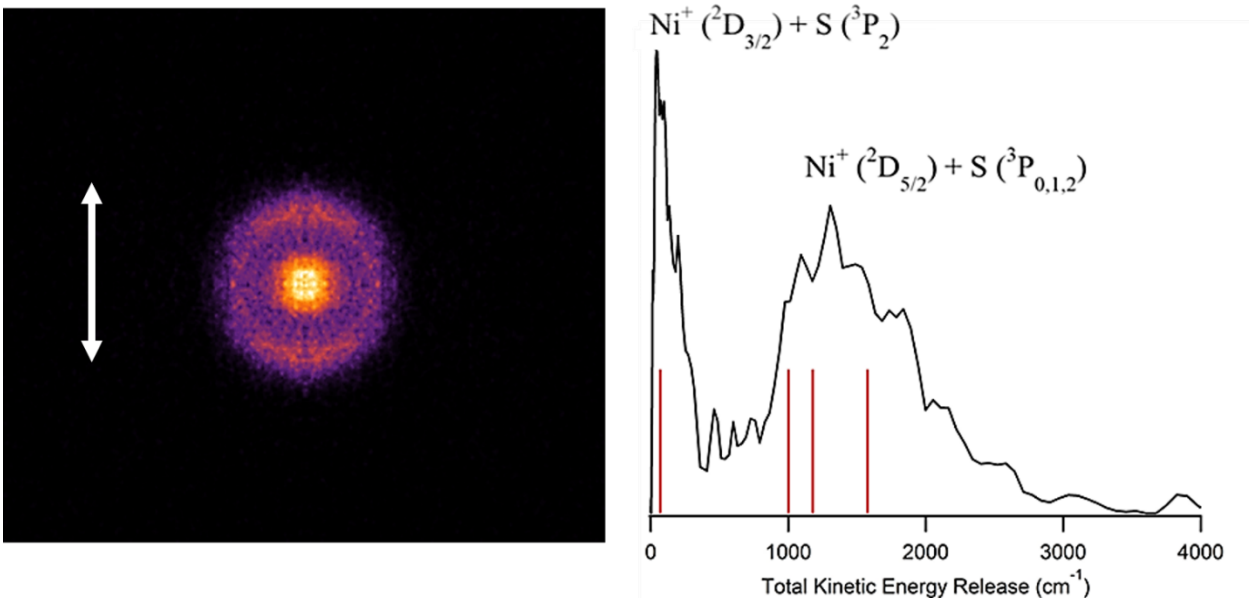

Figure 7. Photofragment image of Ni^+ made by dissociating NiS^+ at 21706 cm^{-1} and the corresponding velocity distribution converted to total kinetic energy release. The image shown has been top/bottom and left/right symmetrized. Laser polarization is vertical (white arrow). Product state reference points along the TKER axis (red vertical lines) are calculated by subtracting the measured D_0 (20090 cm^{-1}) and individual product state energies from the photolysis energy.

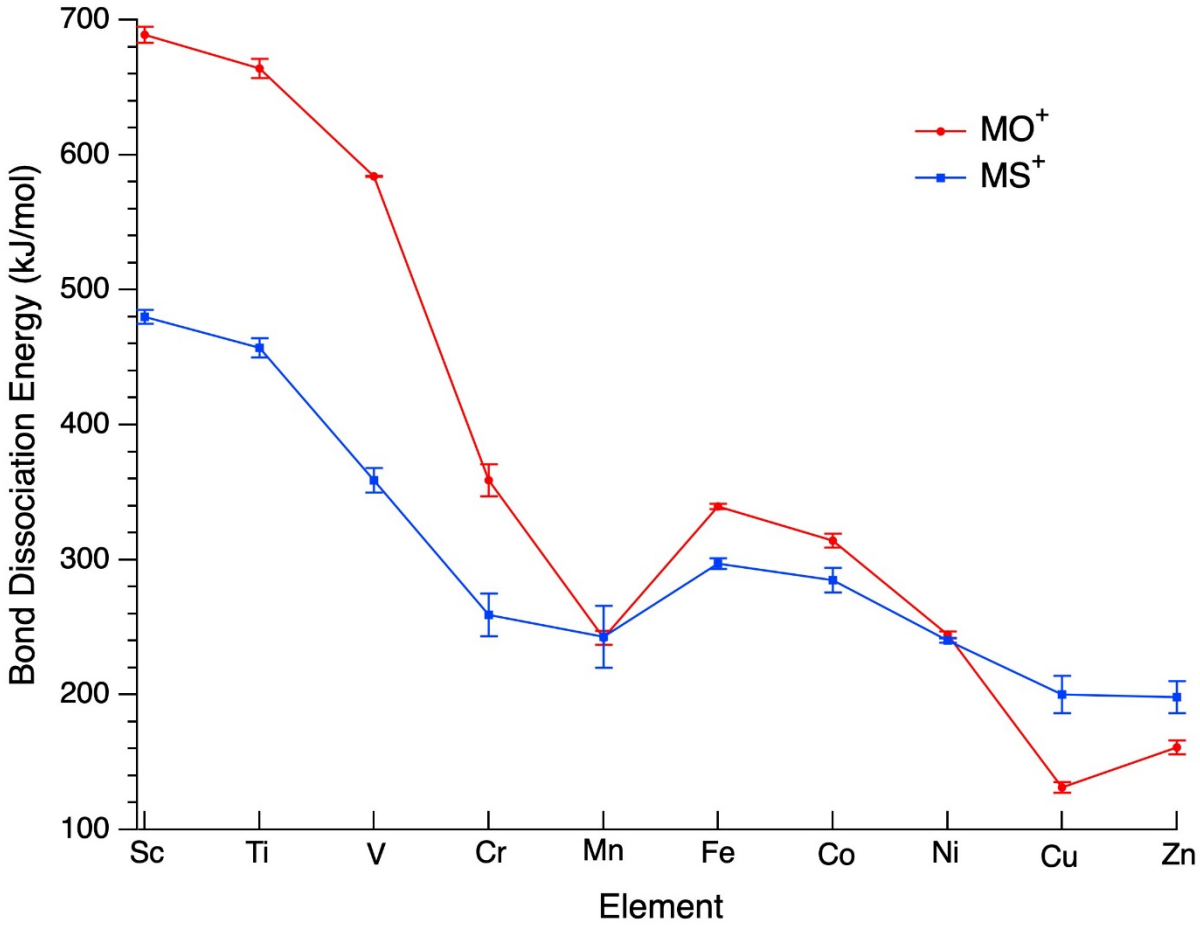

Figure 8. Bond dissociation energies of 3d transition metal oxide (red) and sulfide (blue) cations (plotted from values in Table 3).

References

(1) Schröder, D.; Schwarz, H. FeO^+ Activates Methane. *Angew. Chem. Intl. Ed. Engl.* **1990**, *29*, 1433–1434.

(2) Schröder, D.; Schwarz, H. C-H and C-C Bond Activation by Bare Transition-Metal Oxide Cations in the Gas Phase. *Angew. Chem. Intl. Ed. Engl.* **1995**, *34*, 1973–1995.

(3) Schröder, D.; Schwarz, H.; Clemmer, D. E.; Chen, Y.; Armentrout, P. B.; Baranov, V.; Böhme, D. K. Activation of Hydrogen and Methane by Thermalized FeO^+ in the Gas Phase as Studied by Multiple Mass Spectrometric Techniques. *Int. J. Mass Spectrom. Ion Proc.* **1997**, *161*, 175–191.

(4) Roithova, J.; Schröder, D. Selective Activation of Alkanes by Gas-Phase Metal Ions. *Chem. Rev.* **2010**, *110*, 1170–1211.

(5) Bozovic, A.; Feil, S.; Koyanagi, G. K.; Viggiano, A. A.; Zhang, X.; Schlangen, M.; Schwarz, H.; Bohme, D. K. Conversion of Methane to Methanol: Nickel, Palladium, and Platinum d^9 Cations as Catalysts for the Oxidation of Methane by Ozone at Room Temperature. *Chem.-Eur. J.* **2010**, *16*, 11605–11610.

(6) Dietl, N.; van der Linde, C.; Schlagen, M.; Beyer, M. K.; Schwarz, H. The Final Piece in an Intruiging Puzzle: Bare $[CuO]^+$ and Its Role in the Spin-Selective Hydrogen- and Oxygen-Atom Transfers in Thermal Activation of Methane. *Angew. Chem. Intl. Ed. Engl.* **2011**, *50*, 4966–4969.

(7) Schwarz, H. Chemistry with Methane, Concepts Rather than Recipes. *Angew. Chem. Intl. Ed.* **2011**, *50*, 10096–10115.

(8) McDonald II, D. C.; Sweeny, B. C.; Ard, S. G.; Melko, J. J.; Ruliffson, J. E.; White, M. C.; Viggiano, A. A.; Shuman, N. S. Temperature and Isotope Dependent Kinetics of Nickel-Catalyzed Oxidation of Methane by Ozone. *J. Phys. Chem. A* **2018**, *122*, 6655–6662.

(9) Ard, S. G.; Viggiano, A. A.; Shuman, N. S. Old School Techniques with Modern Capabilities: Kinetics Determination of Dynamical Information Such as Barriers, Multiple

Entrance Channel Complexes, Product States, Spin Crossings, and Size Effects in Metallic Ion–Molecule Reactions. *J. Phys. Chem. A* **2021**, *125*, 3503–3527.

(10) Jackson, T. C.; Carlin, T. J.; Freiser, B. S. Gas-Phase Reactions of MS+ Ions (M = Fe, Co, Ni) with Alkanes. An FTMS Study. *Int. J. Mass Spectrom. Ion Proc.* **1986**, *72*, 169–185.

(11) Nakao, Y.; Hirao, K.; Taketsugu, T. Theoretical Study of First-Row Transition Metal Oxide Cations. *J. Chem. Phys.* **2001**, *114*, 7935–7940.

(12) Sakellaris, C. N.; Mavridis, A. First Principles Exploration of NiO and Its Ions NiO^+ and NiO^-. *J. Chem. Phys.* **2013**, *138*, 054308.

(13) Husband, J.; Aguirre, F.; Thompson, C. J.; Metz, R. B. Photodissociation Spectra of Transition Metal Sulfides: Spin–orbit Structure in Charge Transfer Bands of FeS^+ and NiS^+. *Chem. Phys. Lett.* **2001**, *342*, 75–84.

(14) Lakuntza, O.; Matxain, J. M.; Ugalde, J. M. Quantum Chemical Study of the Reaction between Ni^+ and H_2S. *ChemPhysChem* **2010**, *11*, 3172–3178.

(15) Fisher, E. R.; Elkind, J. L.; Clemmer, D. E.; Georgiadis, R.; Loh, S. K.; Aristov, N.; Sunderlin, L. S.; Armentrout, P. B. Reactions of Fourth-Period Metal Ions (Ca^+-Zn^+) with O_2: Metal-Oxide Ion Bond Energies. *J. Chem. Phys.* **1990**, *93*, 2676–2691.

(16) Vardhan, D.; Liyanage, R.; Armentrout, P. B. Guided Ion Beam Studies of the Reactions of Ni_n^+ (N=2–18) with O_2: Nickel Cluster Oxide and Dioxide Bond Energies. *J. Chem. Phys.* **2003**, *119*, 4166–4178.

(17) Rue, C.; Armentrout, P. B.; Kretzschmar, I.; Schröder, D.; Schwarz, H. Guided Ion Beam Studies of the Reactions of Ni^+, Cu^+, and Zn^+ with CS_2 and COS. *J. Phys. Chem. A* **2002**, *106*, 9788–9797.

(18) Bones, D. L.; Daly, S. M.; Mangan, T. P.; Plane, J. M. C. A Study of the Reactions of Ni^+ and NiO^+ Ions Relevant to Planetary Upper Atmospheres. *Phys. Chem. Chem. Phys.* **2020**, *22*, 8940–8951.

(19) Kang, H.; Beauchamp, J. L. Gas-Phase Studies of Alkene Oxidation by Transition-Metal

Oxides. Ion-Beam Studies of CrO^+. *J. Am. Chem. Soc.* **1986**, *108*, 5663–5668.

(20) Clemmer, D. E.; Dalleska, N. F.; Armentrout, P. B. Reaction of Zn^+ with NO_2. The Gas-Phase Thermochemistry of ZnO. *J. Chem. Phys.* **1991**, *95*, 7263–7268.

(21) Clemmer, D. E.; Elkind, J. L.; Aristov, N.; Armentrout, P. B. Reaction of Sc^+, Ti^+, and V^+ with CO. MC^+ and MO^+ Bond Energies. *J. Chem. Phys.* **1991**, *95*, 3387–3393.

(22) Clemmer, D. E.; Aristov, N.; Armentrout, P. B. Reactions of ScO^+, TiO^+, and VO^+ with D_2: M^+-OH Bond Energies and Effects of Spin Conservation. *J. Phys. Chem.* **1993**, *97*, 544–552.

(23) Metz, R. B.; Nicolas, C.; Ahmed, M.; Leone, S. R. Direct Determination of the Ionization Energies of FeO and CuO with VUV Radiation. *J. Chem. Phys.* **2005**, *123*, 114313.

(24) Parry, I. S.; Hermes, A. C.; Kartouzian, A.; Mackenzie, S. R. Imaging the Photodissociation Dynamics of Neutral Metal Clusters: Copper Dimer, Cu_2 , and Copper Oxide, CuO. *Phys. Chem. Chem. Phys.* **2014**, *16*, 458–466.

(25) Johnston, M. D.; Gentry, M. R.; Metz, R. B. Photofragment Imaging, Spectroscopy and Theory of MnO^+. *J. Phys. Chem. A* **2018**, *122*, 8047–8053.

(26) Merriles, D. M.; Sevy, A.; Nielson, C.; Morse, M. D. The Bond Dissociation Energy of VO Measured by Resonant Three-Photon Ionization Spectroscopy. *J. Chem. Phys.* **2020**, *153*, 024303.

(27) Kretzschmar, I.; Schröder, D.; Schwarz, H.; Rue, C.; Armentrout, P. B. Experimental and Theoretical Studies of Vanadium Sulfide Cation. *J. Phys. Chem. A* **1998**, *102*, 10060–10073.

(28) Kretzschmar, I.; Schroder, D.; Schwarz, H.; Rue, C.; Armentrout, P. B. Thermochemistry and Reactivity of Cationic Scandium and Titanium Sulfide in the Gas Phase. *J. Phys. Chem. A* **2000**, *104*, 5046–5058.

(29) Rue, C.; Armentrout, P. B.; Kretzschmar, I.; Schröder, D.; Schwarz, H. Guided Ion Beam Studies of the State-Specific Reactions of Cr^+ and Mn^+ with CS_2 and COS. *Int. J. Mass*

Spectrom. **2001**, *210/211*, 283–301.

(30) Rue, C.; Armentrout, P. B.; Kretzschmar, I.; Schröder, D.; Schwarz, H. Guided Ion Beam Studies of the Reactions of Fe^+ and Co^+ with CS_2 and COS. *J. Phys. Chem. A* **2001**, *105*, 8456–8464.

(31) Hettich, R. L.; Jackson, T. C.; Stanko, E. M.; Freiser, B. S. Gas-Phase Photodissociation of Organometallic Ions: Bond Energy and Structure Determinations. *J. Am. Chem. Soc.* **1986**, *108*, 5086–5093.

(32) Chandler, D. W.; Houston, P. L. Two-Dimensional Imaging of State-Selected Photodissociation Products Detected by Multiphoton Ionization. *J. Chem. Phys.* **1987**, *87*, 1445–1447.

(33) Eppink, A. T. J. B.; Parker, D. H. Velocity Map Imaging of Ions and Electrons Using Electrostatic Lenses: Application in Photoelectron and Photofragment Ion Imaging of Molecular Oxygen. *Rev. Sci. Instrum.* **1997**, *68*, 3477–3484.

(34) Suits, A. G.; Continetti, R. E. Imaging in Chemical Dynamics. *ACS Symposium Series 770*. American Chemical Society: Washington DC 2000.

(35) Whitaker, B. J. Imaging in Molecular Dynamics: Technology and Applications. Cambridge University Press: New York 2003.

(36) Ashfold, M. N. R.; Nahler, N. H.; Orr-Ewing, A. J.; Vieuxmaire, O. P. J.; Toomes, R. L.; Kitsopoulos, T. N.; Garcia, I. A.; Chestakov, D. A.; Wu, S. M.; Parker, D. H. Imaging the Dynamics of Gas-Phase Reactions. *Phys. Chem. Chem. Phys.* **2006**, *8*, 26–53.

(37) Cooper, G. A.; Gentleman, A. S.; Iskra, A.; Mackenzie, S. R. Photofragmentation Dynamics and Dissociation Energies of MoO and CrO. *J. Chem. Phys.* **2017**, *147*, 13921–13928.

(38) Singh, P. C.; Shen, L.; Kim, M. H.; Suits, A. G. Photodissociation and Photoelectron Imaging of Molecular Ions: Probing Multisurface and Multichannel Dynamics. *Chem. Sci.* **2010**, *1*, 552–560.

(39) Zhang, C.; Li, J.; Zhang, Q.; Chen, Y.; Huang, C.; Yang, X. Mode Specific Photodissociation of CS_2^+ via the $A^2\Pi_u$ State: A Time-Sliced Velocity Map Imaging Study. *Phys. Chem. Chem. Phys.* **2012**, *14*, 2468–2474.

(40) Gardiner, S. H.; Karsili, T. N. V; Lipciuc, M. L.; Wilman, E.; Ashfold, M. N. R.; Vallance, C. Fragmentation Dynamics of the Ethyl Bromide and Ethyl Iodide Cations: A Velocity-Map Imaging Study. *Phys. Chem. Chem. Phys.* **2014**, *16*, 2167–2178.

(41) Johnston, M. D.; Pearson III, W. L.; Wang, G.; Metz, R. B. A Velocity Map Imaging Mass Spectrometer for Photofragments of Fast Ion Beams. *Rev. Sci. Instrum.* **2018**, *89*, 014102.

(42) Johnston, M. D.; Lockwood, S. P.; Metz, R. B. Photofragment Imaging and Electronic Spectroscopy of Al_2^+. *J. Chem. Phys.* **2018**, *148*, 214307–214308.

(43) Rittgers, B. M.; Leicht, D.; Duncan, M. A. Cation−π Complexes of Silver Studied with Photodissociation and Velocity-Map Imaging. *J. Phys. Chem. A* **2020**, *124*, 9166–9186.

(44) Nakashima, Y.; Ito, Y.; Kominato, M.; Ohshimo, K.; Misaizu, F. Photofragment Ion Imaging in Vibrational Predissociation of the H_2O^+Ar Complex Ion. *J. Chem. Phys.* **2021**, *154*, 174301.

(45) Li, W.; Chambreau, S. D.; Lahankar, S. A.; Suits, A. G. Megapixel Ion Imaging with Standard Video. *Rev. Sci. Instrum.* **2005**, *76*, 063106.

(46) Dribinski, V.; Ossadtchi, A.; Mandelshtam, V. A.; Reisler, H. Reconstruction of Abel-Transformable Images: The Gaussian Basis-Set Expansion Abel Transform Method. *Rev. Sci. Instrum.* **2002**, *73*, 2634.

(47) Roberts, G. M.; Nixon, J. L.; Lecointre, J.; Wrede, E.; Verlet, J. R. R. Toward Real-Time Charged-Particle Image Reconstruction Using Polar Onion-Peeling. *Rev. Sci. Instrum.* **2009**, *80*.

(48) Werner, H.-J.; Knowles, P. J.; Knizia, G.; Manby, F. R.; Schütz, M. Molpro: A General-Purpose Quantum Chemistry Program Package . *WIREs Comput. Mol. Sci.* . pp 242–253.

(49) Werner, H.-J.; Knowles, P. J.; Knizia, G.; Manby, F. R.; Schütz, M.; Celani, P.; Györffy, W.; Kats, D.; Korona, T.; Lindh, R. et al, M. MOLPRO, Version 2015.1, a Package of Ab Initio Programs . 2015.

(50) Sousa, C.; de Jong, W. A.; Broer, R.; Nieuwpoort, W. C. Theoretical Characterization of the Low-Lying Excited States of the CuCl Molecule. *J. Chem. Phys.* **1997**, *106*, 7162–7169.

(51) Harrison, J. F. Electronic Structure of Diatomic Molecules Composed of a First-Row Transition Metal and Main-Group Element (H-F). *Chem. Rev.* **2000**, *100*, 679–716.

(52) Kramida, A.; Ralchenko, Y.; Reader, J.; NIST ASD Team. NIST Atomic Spectra Database (Version 5.5.2) http://physics.nist.gov/asd.

(53) Beckert, M.; Greaves, S. J.; Ashfold, M. N. R. High Resolution Ion Imaging Studies of the Photodissociation of the Br_2^+ Cation. *Phys. Chem. Chem. Phys.* **2003**, *5*, 308–314.

(54) Matthew, D. J.; Tieu, E.; Morse, M. D. Determination of the Bond Dissociation Energies of FeX and NiX (X = C, S, Se). *J. Chem. Phys.* **2017**, *146*, 144310.

(55) Anderson, A. B.; Hong, S. Y.; Smialek, J. L. Comparison of Bonding in First Transition-Metal Series: Diatomic and Bulk Sulfides and Oxides. *J. Phys. Chem.* **1987**, *91*, 4250–4254.

(56) Bauschlicher, C. W.; Maitre, P. Theoretical Study of the First Transition Row Oxides and Sulfides. *Theor. Chim. Acta* **1995**, *90*, 189–203.

(57) Bridgeman, A. J.; Rothery, J. Periodic Trends in the Diatomic Monoxides and Monosulfides of the 3d Transition Metals. *J. Chem. Soc., Dalt. Trans.* **2000**, 211–218.

(58) Flory, M. A.; McLamarrah, S. K.; Ziurys, L. M. High-Resolution Spectroscopy of CoS ($X^4\Delta_i$): Examining 3d Transition-Metal Sulfide Bonds. *J. Chem. Phys.* **2005**, *123*, 164312.

(59) Yu, S.; Gordon, I. E.; Sheridan, P. M.; Bernath, P. F. Infrared Emission Spectroscopy of the $A^4\Phi_i$-$X^4\Delta_i$ and $B^4\Pi_i$-$X^4\Delta_i$ Transitions of CoS. *J. Mol. Spectrosc.* **2006**, *236*, 255–259.

(60) Zhen, J. F.; Wang, L.; Qin, C. B.; Zhang, Q.; Chen, Y. Laser-Induced Fluorescence

Spectrum of CoS between 15200 and 19000 Cm^{-1}. *Chin. J. Chem. Phys.* **2010**, *23*, 262–268.

(61) Zhen, J.; Wang, L.; Qin, C.; Chen, Y. Three New Electronic Transitions of CoS Probed by LIF and DF Spectroscopy. *J. Mol. Spectrosc.* **2013**, *290*, 18–23.

(62) Zang, J. Z.; Zhang, Q.; Zhang, D. P.; Qin, C. B.; Zhang, Q.; Chen, Y. Laser-Induced Fluorescence Spectroscopy of CoS: Identification of a New Excited State Arising from the Ground State. *Chin. J. Chem. Phys.* **2013**, *26*, 701–704.

(63) Schröder, D.; Schwarz, H.; Shaik, S. Characterization, Orbital Description, and Reactivity Patterns of Transition-Metal Oxo Species in the Gas Phase. In *Metal-Oxo and Metal-Peroxo Species in Catalytic Oxidations*; Meunier, B., Ed.; Springer Berlin Heidelberg: Berlin, Heidelberg, 2000; pp 91–123.

(64) Miliordos, E.; Mavridis, A. Electronic Structure and Bonding of the Early 3d-Transition Metal Diatomic Oxides and Their Ions: $ScO^{0,\pm}$, $TiO^{0,\pm}$, $CrO^{0,\pm}$, and $MnO^{0,\pm}$. *J. Phys. Chem. A* **2010**, *114*, 8536–8572.

(65) Sorensen, J. J.; Tieu, E.; Sevy, A.; Merriles, D. M.; Nielson, C.; Ewigleben, J. C.; Morse, M. D. Bond Dissociation Energies of Transition Metal Oxides: CrO, MoO, RuO, and RhO. *J. Chem. Phys.* **2020**, *153*, 074303.

TOC Graphic

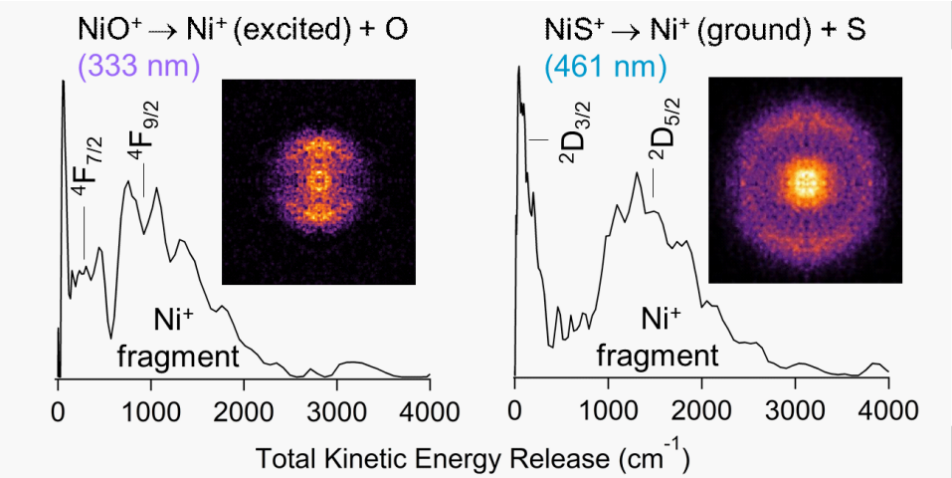
NiO+ → Ni+ (excited) + O
(333 nm)
4F7/2
4F9/2
Ni+
fragment
0
1000
2000
3000
4000
NiS+ → Ni+ (ground) + S
(461 nm)
2D3/2
2D5/2
Ni+
fragment
0
1000
2000
3000
4000
Total Kinetic Energy Release (cm-1)